Admittance Control Scheme Comparison of EXO-UL8: A Dual-Arm Exoskeleton Robotic System

Yang Shen[1], Jianwei Sun[2], Ji Ma[1], Jacob Rosen[1]

Abstract— In physical rehabilitation, exoskeleton assistive devices aim to restore lost motor functions of a patient suffering from neuromuscular or musculoskeletal disorders. These assistive devices are classified as operating in one of two modes: (1) passive mode, in which the exoskeleton passively moves its joints through the full range (or a subset) of the patient's motion during engagement, or (2) assist-as-needed (AAN) mode, in which the exoskeleton provides assistance to the joints of the patient, either by initiating the movements or assisting the patient's movements to complete the task at hand. Achieving high physical human-robot interaction (pHRI) transparency is an open problem for multiple degrees-of-freedom (DOFs) redundant exoskeletons. Using the EXO-UL8 exoskeleton, this study compares two multi-joint admittance control schemes (hyper parameter- based, and Kalman Filter-based) with comfort optimization to improve human-exoskeleton transparency. The control schemes were tested by three healthy subjects who completed reaching tasks while assisted by the exoskeleton. Kinematic information in both joint and task space, as well as force- and torque-based power exchange between the human arm and exoskeleton, are collected and analyzed. The results show that the preliminary Kalman Filter-based control scheme matches the performance of the existing hyper parameter-based scheme, highlighting the potential of the Kalman Filter-based approach for additional performance.

Index Terms— Rehabilitation robotics, upper-limb exoskeleton, admittance control, Kalman Filter, physical human-robot interaction (pHRI), wearable robot.

I. INTRODUCTION

A. Background and Motivation

Every year there are approximately 800,000 new stroke patients in the US with many of them suffering from various disabilities [1]. As a result of brain lesions, stroke victims often lose part of upper-limb motor capabilities, such as the ability to lift their arms up [2]. For decades, engineers and physical therapists have been developing robots to automate the post-stroke training process, resulting in a shift in research trend from low-dimensional, end-effector style "*manipulanda*" to high-dimensional, fully-covered "*exoskeletons*", which can simultaneously manipulate the multiple degrees-of-freedom (DOFs) of the human arm as well as provide additional features, such as tunnel-like force fields and gravity compensation [3]. However, as the upper limb multi-joint coordination strategies and response mechanism to external resistance are not well understood, designing
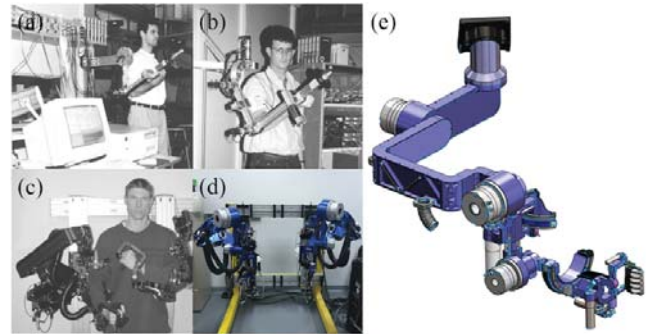

Fig. 1. The EXO-UL exoskeleton series: (a) 1-DOF EXO-UL1; (b) 3-DOF EXO-UL3; (c) 7-DOF dual-arm EXO-UL7; (d) 8-DOF dual-arm EXO-UL8; (e) CAD rendering of the EXO-UL8 [11]

an intelligent exoskeleton controller is not easy [4]. On the other hand, the role of exoskeletons is evolving from "*purely assistive*" to "*training*", since providing excessive assistance to patients during rehabilitation limits the training effectiveness [5]. To increase patients' engagement, better *assist-as-needed* (AAN) algorithms are needed [6]. However, to achieve good performance for AAN algorithms, one first needs to ensure a high human-exoskeleton transparency, i.e., when a patient no longer needs assistance, the exoskeleton should perfectly detect the patient's intention and follow the movement, rather than apply unwanted resistance, which may alter the natural moving patterns. Previous work in intention detection [7], multi-joint coordination [8], adaptive systems and human adaptation [9] has aimed to improve human-exoskeleton transparency. Exoskeleton modeling and simulation have also improved (e.g., MuJoCo [10]), but benefits are more prominent in lower limb applications due to the cyclic movement patterns of walking and constraints imposed by the ground.

B. Objective and Contribution

The exoskeleton system developed at the Bionics lab (Fig. 1) has evolved from 1-DOF, 3-DOF, 7-DOF EXO-UL7 (aka CADEN-7, cable-driven and backdrivable), to the current 8-DOF EXO-UL8 (motor-gear, nonbackdrivable). The purpose of this pilot study is to further improve the human-exoskeleton transparency based on our existing admittance controller.

In the process of improving compliance while maintaining system stability, there are nonlinearities, unpredicted variations, and uncertainties, which are difficult to model/estimate:

[1]Yang Shen, Ji Ma, and Jacob Rosen are with Department of Mechanical and Aeropsace Engineering, University of California Los Angeles, Los Angeles, USA 90095 `yangshen@ucla.edu, jima@ucla.edu, jacobrosen@ucla.edu`

[2]Jianwei Sun is with the Department of Information Technology and Electrical Engineering, ETH Zürich, 8037 Zürich, Switzerland. `jiansun@ethz.ch`
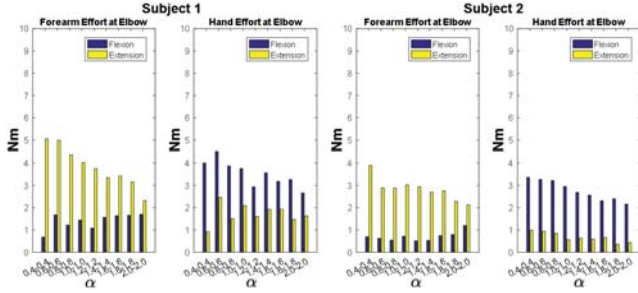
Fig. 2. Effort needed to actuate an exoskeleton is different among subjects, as well as moving directions (e.g., elbow flexion and extension). Data is from two healthy subjects.

Fig. 3. Comparison of admittance control schemes. Scheme A combines the contributions of the force sensors using a weighted sum (hyper gains), while Scheme B estimates the human-applied joint torques with a Kalman Filter.

- The physical human-robot interaction interface (soft hand-cuffs attached to force/torque sensors) brings users "wearable" comfort but introduces nonlinearities
- Tissues (i.e., skin and muscles) surrounding the bones, deform when a human moves his/her arm, and add uncertainties to the interface attached to the arm [12]
- Human motion pattern varies from subject to subject, even from direction to direction (Fig. 2)

Kalman Filter-related techniques were previous used to utilize sEMG or EEG signals as the primary command signals with lower limb or low-DOF non-redundant upper limb exoskeletons [13]–[15]. The utilization of Kalman Filter techniques in the context of high-DOF, redundant, upper limb exoskeleton control, with force/torque as the only sensor input is a unique effort and one of the contributions of this research effort. The Kalman Filter-based admittance control scheme is also compared with the existing hyper parameter-based scheme to assess the exoskeleton's performance.

II. SYSTEM ARCHITECTURE OF THE EXO-UL8

A. Mechanical Design

The mechanical design of EXO-UL8's right side is depicted in Fig. 1(e) [11]. Similar to its predecessor, the EXO-UL8 covers all seven (7) main DOFs of a human's upper limb with each of its two arms, as well as provide an additional hand gripper DOF at the distal end of each arm. Since the opening and closing of the hand has little effect on the arm configuration compared to the other DOFs, this paper focuses on the admittance control of only the first seven DOFs. The design of the EXO-UL8 shifted from a cable-driven actuation mechanism that was implemented in the EXO-UL7 to electric drives for several reasons: a) increased torque outputs enable abnormal movement correction as well as gravity compensation; b) more accurate low-level control can be achieved without unwanted compliance/delay; c) acceptable torque/volume ratio. For each arm, two (2) harmonic drive (Harmonic Drive Systems Inc., Japan) servo systems and one (1) DC motor (Maxon Motor, Swiss) are equipped with encoders and brakes to facilitate movement for the first three DOFs at the shoulder joint (joint 1: abduction/adduction, joint 2: flexion/extension, joint 3: internal/external rotation) and to enable freezing functionality at emergency configurations. One (1) harmonic drive servo system and four (4)
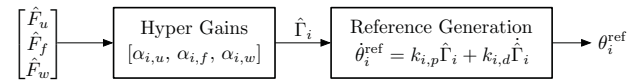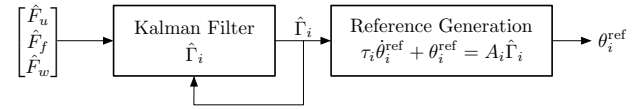
Maxon DC motors are used to realize the five remaining DOFs (joint 4: elbow flexion/extension, joint 5: forearm pronation/supination, joint 6: wrist extension/flexion, joint 7: wrist radial/ulnar deviation, joint 8: hand opening/closing). Three (3) multi-axis F/T sensors (ATI mini 40) are positioned between the human arm and exoskeleton at the handle, forearm and upper arm. One (1) single-axis force sensor is incorporated into the gripper. Details of controller are discussed in Part III.

B. Training Modes

Before the dual-arm system, training modes were limited to pre-defined trajectories or pure-following. Although many studies addressed the assist-as-needed modes for years, generalized findings that can be reused with different systems are limited.

The development of the dual-arm system enabled symmetric mirror image movement training based on between-arm teleoperation. In addition, asymmetric bilateral training using an interactive virtual reality environment was also developed [16]. In either of the training modes and regardless of the motor control functionality level of the human operator, the exoskeleton arm needs to have high "transparency", which means that it is sensitive enough, in a heuristic way, to not exert unwanted resistance on the human arm (otherwise the human's movement, e.g., redundancy resolution, would be affected [17]), as well as be robust enough to prevent instability in all configurations. A trade-off between sensitivity and stability exists, and thus a dynamic equilibrium is needed.

III. ADMITTANCE CONTROL SCHEMES

An admittance controller allows a system to have an arbitrary apparent mechanical admittance by regulating the system's output to a reference trajectory that a virtual system with the desired mechanical admittance would take [18]. The result is that to a human, the system behaves with the desired apparent admittance. In the case of the EXO-UL8 exoskeleton, admittance control allows the exoskeleton's arms to appear much lighter so that the user can easily move them around.

The admittance control scheme implemented consists of two aspects: estimating the torques applied by the human to the exoskeleton's joints, and generating reference trajectories
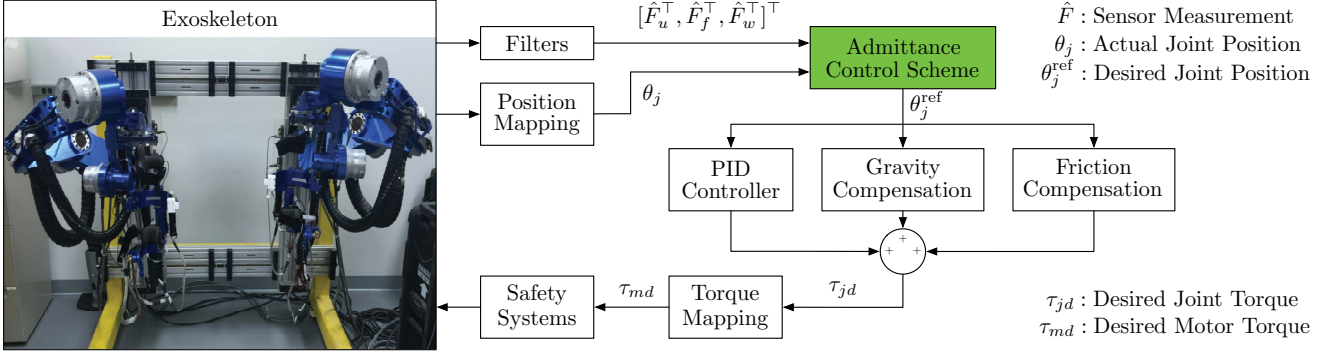
Fig. 4. The exoskeleton controller implements a cascaded control strategy in which low-level motor controllers track references generated by the admittance control scheme. In this comparison study, the green box implements either Scheme A or Scheme B, as discussed in Section III.

for the exoskeleton's joints in response to the human-applied forces. In this study, two admittance control schemes, as shown in Fig. 3, are compared. In Scheme A (the existing control scheme [16]), the human-applied joint torques are calculated from a weighted combination of each sensor's contribution, while in Scheme B, a Kalman Filter is used. In both schemes, the estimated torques are then used to generate an appropriate reference trajectory in joint space so that the exoskeleton appears to have the desired mechanical admittance.

A. Calculating Human-Applied Torques from Sensor Data

Human-applied forces are measured by the force sensors located in the upper arm, lower arm, and wrist handle of the exoskeleton, and are used to calculate the resulting human-applied torques on each of the seven joints. Determining the particular hyper gains for the sensor contributions is a difficult iterative process, which motivated the Kalman Filter as an alternative approach. In either approach, let $\Gamma \in \mathbb{R}^7$ be the actual joint torques resulting from human-applied forces, and $\hat{\Gamma} \in \mathbb{R}^7$ be the estimated joint torques using data from the sensors. Each of the six degrees-of-freedom (DOF) force sensors provides force and torque measurements in the three axes of the sensor's reference frame: $\hat{F} \in \mathbb{R}^6$, $\hat{F} := \text{col}(\hat{f}_x, \hat{f}_y, \hat{f}_z, \hat{\tau}_x, \hat{\tau}_y, \hat{\tau}_z)$. The actual force and torque at each sensor's location, $F \in \mathbb{R}^6$, $F := \text{col}(f_x, f_y, f_z, \tau_x, \tau_y, \tau_z)$, relate to the joint torques through the appropriate Jacobian matrix: $J_u \in \mathbb{R}^{6 \times 7}$ for the upper arm sensor, $J_f \in \mathbb{R}^{6 \times 7}$ for the forearm sensor, and $J_w \in \mathbb{R}^{6 \times 7}$ for the wrist sensor. The generalized force at each sensor is unaffected by joint torques corresponding to joints located past the sensor's position along the exoskeleton arm. As a result, the Jacobians corresponding to the upper and forearm sensors have certain columns that only contain zeros: $(J_u)_{*,4:7} = \mathbb{0}_{6 \times 4}$ and $(J_f)_{*,6:7} = \mathbb{0}_{6 \times 2}$. These Jacobian matrices result in the following relationship between the joint torques and actual generalized forces at each sensor location:

$$\Gamma_{1:3} = (J_u^\top F_u)_{1:3}, \tag{1}$$

$$\Gamma_{1:5} = (J_f^\top F_f)_{1:5}, \tag{2}$$

$$\Gamma_{1:7} = (J_w^\top F_w)_{1:7}. \tag{3}$$

1) Scheme A: Hyper Gains: To address the uncertainties and nonlinearities in multi-joint coordination, hyper gains $\alpha_{j,s}, j \in \{1, \dots, 7\}, s \in \{u, f, w\}$ are introduced:

$$\hat{\Gamma}_j = \alpha_{j,u}\hat{\Gamma}_{j,u} + \alpha_{j,f}\hat{\Gamma}_{j,f} + \alpha_{j,w}\hat{\Gamma}_{j,w}, \tag{4}$$

where $\hat{\Gamma}_{j,s} = (J_s^\top \hat{F}_s)_j$. In a complete form, equation (4) (with the gripper DOF considered separately) is:

$$\begin{bmatrix} \hat{\Gamma}_1 \\ \hat{\Gamma}_2 \\ \hat{\Gamma}_3 \\ \hat{\Gamma}_4 \\ \hat{\Gamma}_5 \\ \hat{\Gamma}_6 \\ \hat{\Gamma}_7 \end{bmatrix} = \begin{bmatrix} \alpha_{1,u}\hat{\Gamma}_{1,u} + \alpha_{1,f}\hat{\Gamma}_{1,f} + \alpha_{1,w}\hat{\Gamma}_{1,w} \\ \alpha_{2,u}\hat{\Gamma}_{2,u} + \alpha_{2,f}\hat{\Gamma}_{2,f} + \alpha_{2,w}\hat{\Gamma}_{2,w} \\ \alpha_{3,u}\hat{\Gamma}_{3,u} + \alpha_{3,f}\hat{\Gamma}_{3,f} + \alpha_{3,w}\hat{\Gamma}_{3,w} \\ \alpha_{4,f}\hat{\Gamma}_{4,f} + \alpha_{4,w}\hat{\Gamma}_{4,w} \\ \alpha_{5,f}\hat{\Gamma}_{5,f} + \alpha_{5,w}\hat{\Gamma}_{5,w} \\ \alpha_{6,w}\hat{\Gamma}_{6,w} \\ \alpha_{7,w}\hat{\Gamma}_{7,w} \end{bmatrix}. \tag{5}$$

Contributions to specific joints could be compromised due to uncertain nonlinearities, which may lead to the coactivation of other exoskeleton DOFs (unwanted movements) during movement. To overcome this unindended effect, the user may be forced to exert additional effort in order to achieve the desired motion.

TABLE I
DIFFERENT JOINT TORQUE LIMITS

Body Part	Max Strength (N-m)	Max Strength (N-m)
Shoulder	Flexion: 13.13	Extension: 8.90
	Adduction: 14.49	Abduction: 15.62
	Internal Rotation: 11.59	External Rotation: 11.63
Elbow	Flexion: 10.75	Extension: 8.76
	Pronation: 3.39	Supination: 1.42
Wrist	Extension: 2.11	Flexion: 1.55
	Radial Deviation: 2.67	Ulnar Deviation: 1.98

To quantify the comfort level (denoted as cl), we normalize the effort at each joint based on [19]:

$$cl_j = 1 - \tau_j/\tau_{j,max}, \ j \in \{1, \dots, 7\}. \tag{6}$$

Note that cl_j is direction-dependent due to the difference in concentric and eccentric contractions. As shown in Table I, the second and third columns list positive and negative

rotations on exoskeleton, respectively. The hyper gains are manually tuned so that the comfort level is approximately optimized. The exoskeleton's gravity and friction are separately compensated.

2) Scheme B: Kalman Filtering: The Kalman Filter approach is based off the work of [18], in which the joint torques to estimate are modeled as entirely driven by Gaussian noise:

$$\dot{\Gamma} = w_\Gamma, \tag{7}$$

where $w_\Gamma \sim \mathcal{N}(\mathbb{0}_{7 \times 1}, Q_\Gamma)$, with Q_Γ being a covariance matrix. Tuning Q_Γ allows tuning how responsive a particular joint is to the human-applied torques. For use in the Kalman Filter, equation (7) is descretized to:

$$\Gamma[k+1] = \Gamma[k] + (\Delta t) w_\Gamma[k], \tag{8}$$

where Δt is the time-step.

Since Γ is the state that the Kalman Filter tries to estimate, equations (1), (2), and (3) provide a measurement model for Γ. At each sampling time-step $k \in \mathbb{Z}$, assume the sensor's measurement data is corrupted with additive Gaussian noise, and let

$$\bar{z}[k] := \begin{bmatrix} (J_u^\top \hat{F}_u)[k] \\ (J_f^\top \hat{F}_f)[k] \\ (J_w^\top \hat{F}_w)[k] \end{bmatrix}. \tag{9}$$

Then,

$$\bar{z}[k] = \begin{bmatrix} \mathbb{I}_{3\times3} & \mathbb{0}_{3\times4} \\ \mathbb{I}_{5\times5} & \mathbb{0}_{5\times2} \\ & \mathbb{I}_{7\times7} \end{bmatrix} \Gamma[k] + \begin{bmatrix} v_u[k] \\ v_f[k] \\ v_w[k] \end{bmatrix}, \tag{10}$$

$$:= H[k]\Gamma[k] + \mathrm{col}(v_u[k], v_f[k], v_w[k]), \tag{11}$$

where $v_u[k] \in \mathbb{R}^3$, $v_u[k] \sim \mathcal{N}(\mathbb{0}_{3\times1}, R_u)$; $v_f[k] \in \mathbb{R}^5$, $v_f[k] \sim \mathcal{N}(\mathbb{0}_{5\times1}, R_f)$; and $v_w[k] \in \mathbb{R}^7$, $v_w[k] \sim \mathcal{N}(\mathbb{0}_{7\times1}, R_w)$.

Equations (8) and (10) are the Kalman Filter's process and measurement models, respectively. At each time-step, the prior and a posteriori updates are performed to yield $\hat{\Gamma}[k]$, which is the minimum mean square error (MMSE) estimate of $\Gamma[k]$. Let P_p be the prior's variance, P_m be the a posteriori's variance, and $R := \mathrm{diag}(R_u, R_f, R_w)$. Then, the update equations of the Kalman Filter for this system in particular are as follows.

Initialization:

$$\hat{\Gamma}[0] = \mathbb{0}_{7\times1}, \tag{12}$$

$$P_m[0] = (\Delta t)^2 Q_\Gamma. \tag{13}$$

Prior Update:

$$P_p[k] = P_m[k-1] + (\Delta t)^2 Q_\Gamma. \tag{14}$$

A Posteriori Update:

$$K[k] = P_p[k]H^\top[k](H[k]P_p[k]H^\top[k] + R)^{-1}, \tag{15}$$

$$\hat{\Gamma}[k] = (\mathbb{I} - K[k]H[k])\hat{\Gamma}[k-1] + K[k]\bar{z}[k], \tag{16}$$

$$P_m[k] = (\mathbb{I} - K[k]H[k])P_p[k](\mathbb{I} - K[k]H[k])^\top \tag{17}$$
$$+ K[k]RK^\top[k].$$

The process and measurement noise covariance matrices are manually tuned in an iterative approach until the exoskeleton's movements are heuristically determined to be smooth, yet responsive. Smaller process noise covariance results in smoother estimated torques, while smaller measurement noise covariance terms for a particular sensor measurement increases its contribution to the estimated torque. Note that the Joseph form is used for the covariance's a posteriori update in equation (17) for numerical stability.

The estimated $\hat{\Gamma}[k]$ is subsequently used to generate the appropriate reference signal in joint space.

B. Joint Space Reference Generation

While second-order models have been used in other studies [18, Eq. 3] [20, Eq. 4], a first-order model was chosen over a second-order model to allow the exoskeleton to be perceived as more responsive to the user.

1) Scheme A: The calculated torque signals are filtered and input into a PD admittance controller:

$$\dot{\theta}_j^{\mathrm{ref}} = k_{j,p}\hat{\Gamma}_j + k_{j,d}\dot{\hat{\Gamma}}_j, \ j \in \{1, \ldots, 7\}, \tag{18}$$

where $k_{j,p}$ and $k_{j,d}$ are manually tuned gains, and each θ_j^{ref} is tracked by the corresponding low-level motor controller.

2) Scheme B: The estimated human-applied joint torques $\hat{\Gamma}$ are used to each drive a first-order reference generation model for the corresponding joint:

$$\tau_j \dot{\theta}_j^{\mathrm{ref}} + \theta_j^{\mathrm{ref}} = A_j\hat{\Gamma}_j, \ j \in \{1, \ldots, 7\}, \tag{19}$$

where τ_j and A_j are the desired time constant and DC gain for the joint, respectively. These parameters are manually tuned to achieve the desired responsiveness of the particular joint. For implementation, equation (19) is discretized using exact discretization to yield:

$$\theta_j^{\mathrm{ref}}[k+1] = e^{-\frac{\Delta t}{\tau_j}}\theta_j^{\mathrm{ref}}[k] + A_j(1 - e^{-\frac{\Delta t}{\tau_j}})\hat{\Gamma}_j[k], \tag{20}$$

for $j \in \{1, \ldots, 7\}$. The generated reference signal, θ^{ref}, is then tracked by the individual motor controllers, as shown in Fig. 4.

IV. EXPERIMENT

This experiment explored the performance of each control scheme through interaction with three healthy subjects, recruited according to an approved IRB protocol (IRB #17-001646). Only the right arm of the exoskeleton was utilized (all subjects are right-handed).

A. Setup

Assistance was provided to help subjects into the exoskeleton and attach the cuffs. Subjects were instructed to wear short-sleeve t-shirts to reduce any nonlinearity effects resulting from deformation of clothing. To eliminate possible perceptual interference imposed by a virtual reality environment feature of the exoskeleton system, the experiment was limited to interaction with real objects only, as shown in Fig. 5(a).

B. Tasks

The subjects wore the exoskeleton and were asked to perform reaching tasks with their right (dominant) arm using a sequence of targets as shown in Fig. 5(b). The #0 target is located at the center of a 3×3 target matrix. The complete experiment task description is illustrated in Algorithm 1.

Algorithm 1: Experiment Protocol on Each Subject

Subject wear the exoskeleton on the dominant arm
  begin
    for $Scheme = A, B$ **do**
      Become familiar with the system for 5min, and rest for 1min
      for $i = 1, 2, ..., 8$ **do**
        Move the tip from Target #0 to Target #i (in 3sec, as instructed by a metronome)
        if *not touched* **then**
          Keep moving
        else
          Move the tip back to Target #0 (in 3sec, instructed by a metronome)
    Take off the exoskeleton, and rest for 5min

C. Data Collection

Both kinematic and force data were collected: joint position was recorded from the optical encoders at the seven motors on the exoskeleton arm at 100Hz; force/torque information, $\hat{F}$, was measured by the three sensors on the exoskeleton arm at 100Hz as well.

V. RESULTS

Several aspects of the subjects physical interaction with EXO-UL8 are quantitatively analyzed and discussed below to compare the controllers' performance.
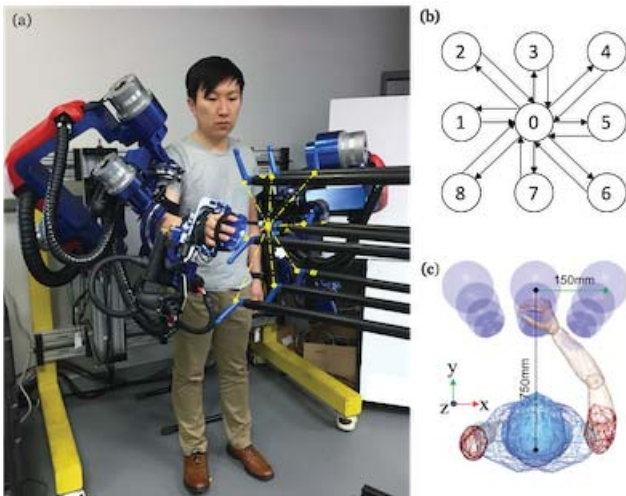

Fig. 5. Experiment setup: (a) A subject is wearing the exoskeleton to accomplish trajectory tracking tasks; (b) Planned trajectory (detailed in Algorithm 1); (c) Top view of the experiment setup.
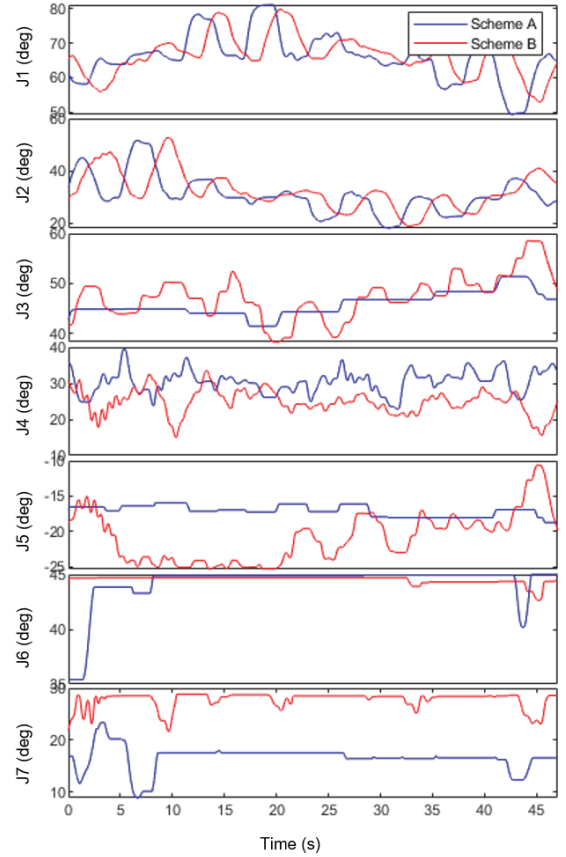

Fig. 6. Joint space position trajectory of Subject 1 under Schemes A and B. Although completion time and task space error (Table II) are comparable, joint usage preference differs. Joints 3 and 5 are used less in Scheme A than in Scheme B. The Kalman filter better estimates supination/pronation (joint 5) and shoulder internal/external rotation (joint 3).

A. High-Level Trajectory Tracking - Joint Space

1) Joint space position trajectory: Joint space position trajectories of all seven DOFs of Subject #1 are depicted in Fig. 6. The summary of joint position distribution is shown in Fig. 7(a). Comparison of the joint space trajectories indicates the differences between the two control schemes in joint usage preference.

2) Joint space jerkiness: As observed in the distribution in Fig. 7(b), the joint space jerk (third-order time derivative of joint position or first time derivative of the angular acceleration) in both Scheme A and Scheme B are comparable, indicating similar performance between the control schemes in terms of providing smooth trajectory tracking.

B. High-Level Trajectory Tracking - Task Space

1) Task space position trajectory: The position over time of the end-effector in task space for both admittance control schemes is shown in Fig. 8. By qualitative observation, both admittance control schemes are adequate in responding to the estimated human-applied torques by moving the exoskeleton to the desired positions.
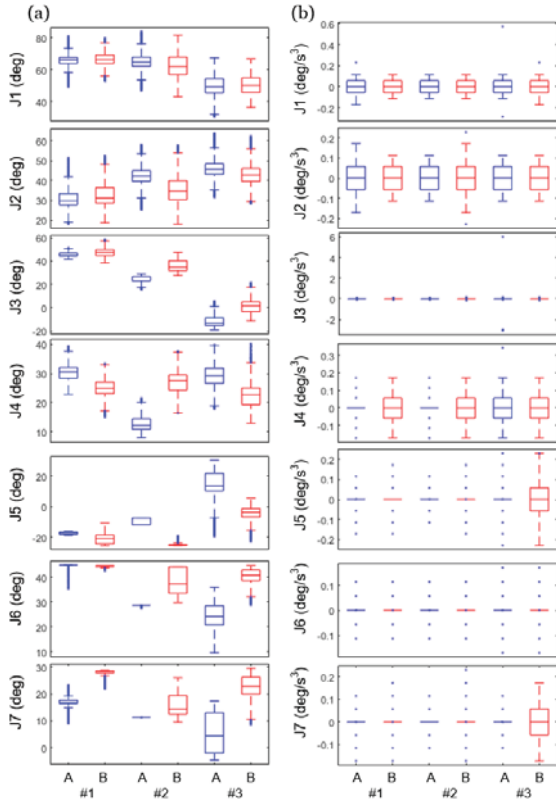
Fig. 7.   Joint space position (a) and joint space jerkiness (b) distributions of all subjects under Scheme A and Scheme B.
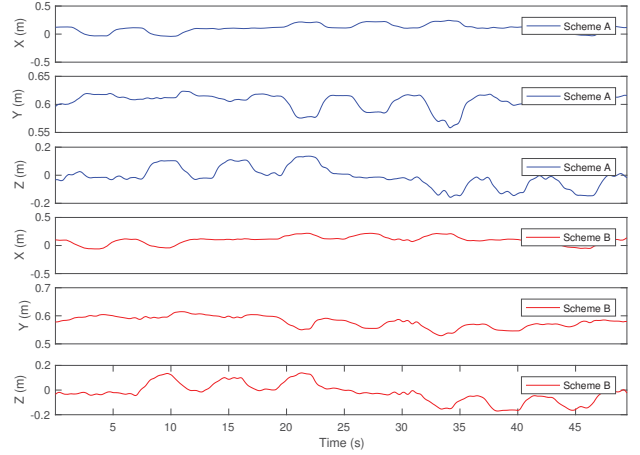

Fig. 8.   Task Space Position Trajectory of Subject 1, under Scheme A and B. Both control schemes show satisfactory functionality for the duration of the test time. Similar observations were made for all three test subjects.
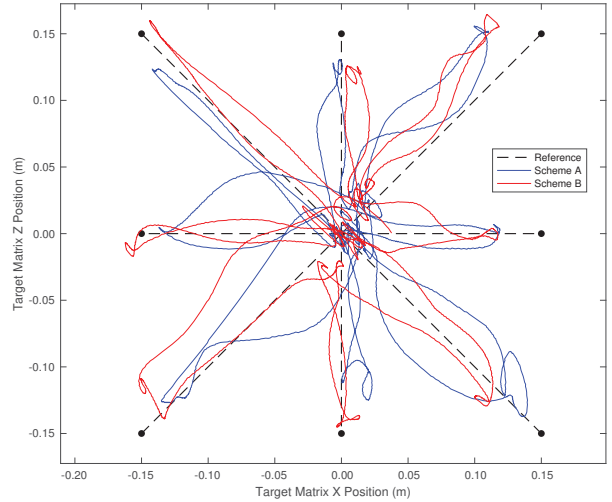

Fig. 9.   Task Space Reference Following of Subject 1, under Scheme A and B. Both control schemes show similar magnitudes of error in guiding the exoskeleton's end-effector along the reference trajectories.

2) Task space error: The task space error for each subject under each admittance control scheme is the total deviation of the actual human controlled trajectory from the reference trajectory of Fig. 5 (b). A sample plot of Subject 1's trajectory in the plane of the target matrix is shown in Fig. 9. To quantify the error, let it be defined as the root-mean-square (RMS) of the minimum distance of the actual trajectory to the reference trajectory summed over all segments of the reference trajectory, similar to the approach presented in [17]: $\sum_{\gamma \in \text{segments}} \sqrt{(d_{\gamma,1}^2 + \cdots + d_{\gamma,n}^2)/n}$, where $d_{\gamma,i}$ is the minimum distance to segment γ of the reference trajectory. The errors are tabulated in Table II. Both control schemes exhibit similar performance in terms of error magnitude, indicating that task space errors depend more on the operator than the particular admittance control scheme used.

TABLE II

TASK SPACE ERRORS UNDER BOTH SCHEMES FOR EACH SUBJECT

Subject	Scheme A (unit: m)	Scheme B (unit: m)
1	0.0610	0.0634
2	0.0777	0.0778
3	0.1219	0.1091

C. Power Exchange

The power exchange is the amount of mechanical power the user inputs into the exoskeleton device through the three sensors. Ideally, power exchange is minimal, which is indicative of high human-exoskeleton transparency. The mean power exchange of each test subject for each control scheme is tabulated in Table III, which show a redistribution of the power exchange for each sensor. Scheme B evens out the contributions of the lower and handle sensors more than scheme A, which may indicate more uniform transparency.

VI. CONCLUSIONS

This study compares two different admittance control schemes (existing hyper parameter-based, and Kalman Filter-based) on the EXO-UL8, a dual-arm, high-DOF redundant

TABLE III

MEAN POWER EXCHANGE UNDER BOTH SCHEMES FOR EACH SUBJECT

Subject	Scheme A (unit: mW)			Scheme B (unit: mW)		
	Upper	Lower	Handle	Upper	Lower	Handle
1	89	176	345	155	544	507
2	74	185	248	89	208	200
3	123	210	91	69	203	182

exoskeleton system for upper-limb post-stroke rehabilitation. The device's functionality in facilitating single movements based on three healthy subjects' pHRI was experimentally validated and quantitative data, such as joint space/task space trajectories and human-exoskeleton power exchange, was analyzed. Results show promising performance in terms of functionality, human-exoskeleton transparency, reference-following error, and mechanical power exchange. The proposed control schemes will continue to be further investigated and modified for additional features (e.g., a multi-finger hand exoskeleton under development [21]).

REFERENCES

[1] E. J. Benjamin, M. J. Blaha, S. E. Chiuve, M. Cushman, S. R. Das, R. Deo, S. D. de Ferranti, J. Floyd, M. Fornage, C. Gillespie, C. R. Isasi, M. C. Jiménez, L. C. Jordan, S. E. Judd, D. Lackland, J. H. Lichtman, L. Lisabeth, S. Liu, C. T. Longenecker, R. H. Mackey, K. Matsushita, D. Mozaffarian, M. E. Mussolino, M. Nasir, R. W. Neumar, L. Palaniappan, D. K. Pandey, R. R. Thiagarajan, M. J. Reeves, M. Ritchey, C. J. Rodriguez, G. A. Roth, W. D. Rosamond, C. Sasson, A. Towfighi, C. W. Tsao, M. B. Turner, S. S. Virani, J. H. Voeks, J. Z. Willey, J. T. Wilkins, J. H. Wu, H. M. Alger, S. S. Wong, and P. Muntner, "Heart Disease and Stroke Statistics-2017 Update: A Report From the American Heart Association," *Circulation*, vol. 135, pp. e146–e603, 3 2017.
[2] P. Langhorne, J. Bernhardt, and G. Kwakkel, "Stroke rehabilitation," *Lancet*, vol. 377, pp. 1693–1702, 2011.
[3] H. S. Lo and S. Q. Xie, "Exoskeleton robots for upper-limb rehabilitation: State of the art and future prospects," *Medical Engineering & Physics*, vol. 34, no. 3, pp. 261–268, 2012.
[4] N. Jarrassé, T. Proietti, V. Crocher, J. Robertson, A. Sahbani, G. Morel, and A. Roby-Brami, "Robotic exoskeletons: a perspective for the rehabilitation of arm coordination in stroke patients," *Frontiers in Human Neuroscience*, vol. 8, p. 947, 12 2014.
[5] D. J. Reinkensmeyer, E. Burdet, M. Casadio, J. W. Krakauer, G. Kwakkel, C. E. Lang, S. P. Swinnen, N. S. Ward, and N. Schweighofer, "Computational neurorehabilitation: modeling plasticity and learning to predict recovery.," *Journal of neuroengineering and rehabilitation*, vol. 13, no. 1, p. 42, 2016.
[6] A. A. Blank, J. A. French, A. U. Pehlivan, and M. K. O'Malley, "Current Trends in Robot-Assisted Upper-Limb Stroke Rehabilitation: Promoting Patient Engagement in Therapy," *Current physical medicine and rehabilitation reports*, vol. 2, no. 3, pp. 184–195, 2014.
[7] J. Lobo-Prat, P. N. Kooren, A. H. Stienen, J. L. Herder, B. F. Koopman, and P. H. Veltink, "Non-invasive control interfaces for intention detection in active movement-assistive devices," *Journal of NeuroEngineering and Rehabilitation*, vol. 11, no. 1, 2014.
[8] P. Haggard, K. Hutchinson, and J. Stein, "Patterns of coordinated multi-joint movement," *Experimental Brain Research*, vol. 107, pp. 254–266, 12 1995.
[9] L. Peternel, T. Noda, T. Petrič, A. Ude, J. Morimoto, and J. Babič, "Adaptive Control of Exoskeleton Robots for Periodic Assistive Behaviours Based on EMG Feedback Minimisation," *PLOS ONE*, vol. 11, p. e0148942, 2 2016.

[10] E. Todorov, T. Erez, and Y. Tassa, "MuJoCo: A physics engine for model-based control," in *2012 IEEE/RSJ International Conference on Intelligent Robots and Systems*, pp. 5026–5033, IEEE, 10 2012.
[11] Y. Shen, P. W. Ferguson, J. Ma, and J. Rosen, "Chapter 4 - Upper Limb Wearable Exoskeleton Systems for Rehabilitation: State of the Art Review and a Case Study of the EXO-UL8 Dual-Arm Exoskeleton System," in *Wearable Technology in Medicine and Health Care* (R. K.-Y. Tong, ed.), pp. 71–90, Academic Press, 2018.
[12] N. Jarrassé and G. Morel, "Connecting a human limb to an exoskeleton," *IEEE Transactions on Robotics*, vol. 28, no. 3, pp. 697–709, 2012.
[13] Z. Li, B. Wang, F. Sun, C. Yang, Q. Xie, and W. Zhang, "SEMG-based joint force control for an upper-limb power-assist exoskeleton robot," *IEEE Journal of Biomedical and Health Informatics*, vol. 18, no. 3, pp. 1043–1050, 2014.
[14] J. Huang, W. Huo, W. Xu, S. Mohammed, and Y. Amirat, "Control of Upper-Limb Power-Assist Exoskeleton Using a Human-Robot Interface Based on Motion Intention Recognition," *IEEE Transactions on Automation Science and Engineering*, vol. 12, no. 4, pp. 1257–1270, 2015.
[15] A. Kilicarslan, S. Prasad, R. G. Grossman, and J. L. Contreras-Vidal, "High accuracy decoding of user intentions using EEG to control a lower-body exoskeleton," in *2013 35th Annual International Conference of the IEEE Engineering in Medicine and Biology Society (EMBC)*, pp. 5606–5609, IEEE, 7 2013.
[16] Y. Shen, J. Ma, B. Dobkin, and J. Rosen, "Asymmetric Dual Arm Approach For Post Stroke Recovery Of Motor Functions Utilizing The EXO-UL8 Exoskeleton System: A Pilot Study," in *2018 40th Annual International Conference of the IEEE Engineering in Medicine and Biology Society (EMBC)*, vol. 2018, pp. 1701–1707, IEEE, 7 2018.
[17] Y. Shen, B. P.-Y. Hsiao, J. Ma, and J. Rosen, "Upper limb redundancy resolution under gravitational loading conditions: Arm postural stability index based on dynamic manipulability analysis," in *2017 IEEE-RAS 17th International Conference on Humanoid Robotics (Humanoids)*, pp. 332–338, IEEE, 11 2017.
[18] F. Augugliaro and R. D'Andrea, "Admittance control for physical human-quadrocopter interaction," in *2013 European Control Conference (ECC)*, pp. 1805–1810, IEEE, 7 2013.
[19] P. Lee, S. Wei, J. Zhao, and N. I. Badler, "Strength guided motion," *ACM SIGGRAPH Computer Graphics*, vol. 24, no. 4, pp. 253–262, 1990.
[20] B. Huang, Z. Ye, Z. Li, W. Yuan, and C. Yang, "Admittance control of a robotic exoskeleton for physical human robot interaction," in *2017 2nd International Conference on Advanced Robotics and Mechatronics (ICARM)*, (Hefei), pp. 245–250, 2017.
[21] P. W. Ferguson, B. Dimapasoc, Y. Shen, and J. Rosen, "Design of a Hand Exoskeleton for Use with Upper Limb Exoskeletons," in *Wearable Robotics: Challenges and Trends* (M. C. Carrozza, S. Micera, and J. L. Pons, eds.), Biosystems & Biorobotics, pp. 276–280, Cham: Springer International Publishing, 2019.